



OPEN

# Novel calcium hexaluminate/ spinel-alumina composites with graded microstructures and mechanical properties

SUBJECT AREAS:

CERAMICS

MECHANICAL PROPERTIES

Received  
9 December 2013Accepted  
17 February 2014Published  
11 March 2014Correspondence and  
requests for materials  
should be addressed to  
Z.H.H. (huang118@  
cugb.edu.cn)Shuai Yi<sup>1,2</sup>, Zhaohui Huang<sup>1</sup>, Juntong Huang<sup>1,2</sup>, Minghao Fang<sup>1</sup>, Yan'gai Liu<sup>1</sup> & Shaowei Zhang<sup>2</sup><sup>1</sup>School of Materials Science and Technology, China University of Geosciences (Beijing), Beijing 100083, People's Republic of China, <sup>2</sup>College of Engineering, Mathematics and Physical Sciences, University of Exeter, Exeter EX4 4QF, United Kingdom.

Calcium hexaluminate (CA<sub>6</sub>) was incorporated into the matrix of magnesio aluminate spinel-alumina (MA-A) via infiltration of a porous preform fabricated from  $\alpha$ -Al<sub>2</sub>O<sub>3</sub> and MgO powders with a saturated calcium acetate solution and subsequent firing, forming CA<sub>6</sub>/(MA-A) functionally composites with graded fracture toughness. Actually, the porous preform was partially and perpendicularly immersed (1/4 of its length) in the solution. Owing to the capillary action, the calcium acetate solution was absorbed into the porous preform, and the different absorption distance led to the graded solution concentration in the height direction of the porous preform. The *in-situ* formation of CA<sub>6</sub> conferred graded microstructures, as well as improved mechanical properties on the resultant composites. The CA<sub>6</sub> content decreased gradually along the solution absorption direction, *i.e.*, from one end [CA<sub>6</sub>/(MA-A) region] immersed in solution to the other end [MA-A region], reducing evidently the formation of layered structure along the direction, while increasing gradually the formation of spherical alumina particles. The CA<sub>6</sub>/(MA-A) region had a better toughness that could prevent the crack propagation and improve the spalling resistance. Meanwhile, the MA-A region could provide structural support, because of the higher Vickers hardness and density.

Magnesio aluminate spinel (MA) and alumina (A) are important raw materials for advanced refractories and ceramics. The former is extensively used to prepare monolithic refractories because of its superior corrosion resistance and thermal shock resistance, and the latter is widely applied in the areas where the resistances against wear, oxidation, chemical corrosion and/or heat are required<sup>1–6</sup>. Nevertheless, they also suffer from some drawbacks, in particular, the high volume expansion (5%–7%) associated with the formation of MA<sup>7,8</sup>, and a relatively poor thermal shock resistance and low toughness of alumina. A double-stage firing process, *i.e.*, pre-formation at ~1400°C and subsequent densification at ~1700°C, is often employed to prepare dense MA<sup>9</sup>, or additives such as TiO<sub>2</sub>, ZnO, Y<sub>2</sub>O<sub>3</sub>, CaF<sub>2</sub> and Cr<sub>2</sub>O<sub>3</sub> are used to promote its formation and densification<sup>10–13</sup>. In the case of alumina, several methodologies also have been proposed to improve its mechanical properties, including rare-earth element doping<sup>14,15</sup>, metal particle dispersion<sup>16</sup>, heterogeneous microstructure design<sup>17–19</sup>, use of carbon fillers<sup>20–25</sup>, and platelet- and/or needle-like grain reinforcement<sup>26–28</sup>.

Calcium hexaluminate (CaAl<sub>12</sub>O<sub>19</sub>, CA<sub>6</sub>), the most alumina-rich compound in the CaO-Al<sub>2</sub>O<sub>3</sub> system, usually develops a plate-like morphology and is thermodynamically stable up to its peritectic point around 1875°C. These, along with its excellent alkaline resistance, high stability in a reducing atmosphere and low thermal conductivity, make it a promising material for refractory and engine insulation applications. In addition, it can be used to reinforce Al<sub>2</sub>O<sub>3</sub> ceramics because of its platelet morphology, good chemical and thermal compatibilities with Al<sub>2</sub>O<sub>3</sub> (both have similar thermal expansion coefficients,  $\alpha_{CA_6} = 8.0 \cdot 10^{-6} \text{ }^\circ\text{C}^{-1}$  and  $\alpha_A = 8.6 \cdot 10^{-6} \text{ }^\circ\text{C}^{-1}$ )<sup>29–31</sup>. Considering that MA also has a very close thermal expansion coefficient ( $\alpha_{MA} = 8.9 \cdot 10^{-6} \text{ }^\circ\text{C}^{-1}$ ), we propose to incorporate plate-like CA<sub>6</sub> into the MA-A matrix via liquid infiltration and subsequent firing to develop a novel functionally graded composite with improved microstructures and mechanical properties.

The infiltration of porous preforms with suitable liquid or gaseous species is a feasible way to introduce other phases into them<sup>32</sup>, and to design new materials with distinct microstructures and properties<sup>31</sup>. In recent years, with the development of the infiltration technique, alternating laminations of homogeneous and heterogeneous layers in a material has been achieved, conferring a combined wear and fracture resistance on the composites. The

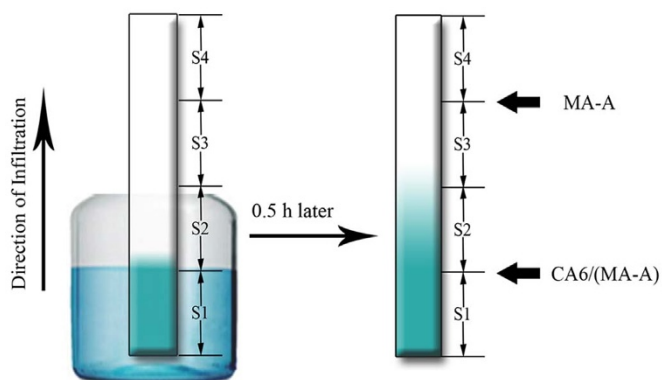


**Figure 1** | A schematic diagram illustrating the typical infiltration process used in this work.

technique has been successfully adopted to fabricate several new graded composites, including mullite/alumina, mullite/zirconia-toughened alumina, aluminium titanate/alumina, calcium hexaluminate/alumina<sup>32–36</sup>.

The main objective of this work is to design functionally graded composites of  $\text{CA}_6/(\text{MA-A})$  with novel microstructures and excellent combined properties of MA spinel, alumina and calcium hexaluminate. A homogeneous layer of MA-A in the composites is designed for wear, corrosion, slag and thermal shock resistance and another heterogeneous layer of  $\text{CA}_6/(\text{MA-A})$  for fracture resistance. In this paper, functionally graded composites of  $\text{CA}_6/(\text{MA-A})$  are prepared through two steps. The first step is the preparation of preform. Then the second step is the fabrication of the  $\text{CA}_6/(\text{MA-A})$ . The main results of the work have been reported. This research may provide a new and simple approach to prepare functionally graded composites with graded microstructures and tailorable or tunable properties.

## Results

**Microstructural characteristic of the preform.** A porous preform is partially immersed (1/4 of its length) in a saturated calcium acetate solution (see Fig. 1 for more details). The SEM images of preform are shown in Fig. 2. The preform was prepared from  $\text{MgO}$  and  $\alpha\text{-Al}_2\text{O}_3$ , and heated at  $1100^\circ\text{C}$  to increase its strength while still maintaining a sufficient level of porosity in it for the infiltration. The open porosity of preform was about 44.55%, and its bulk density was only about  $2.02\text{ g}\cdot\text{cm}^{-3}$ , based on the Archimedes' principle. As shown in Fig. 2, the samples were not sintered yet. There were a large number of connected tiny pores ( $\sim 0.1\ \mu\text{m}$ ) in the preform, forming a lot of capillary.

**Phase compositions of  $\text{CA}_6/(\text{MA-A})$  composites.** XRD patterns of four different sections in the fired sample (S1, S2, S3, S4) are shown in Fig. 3.  $\alpha\text{-Al}_2\text{O}_3$ ,  $\text{MgAl}_2\text{O}_4$  and  $\text{CaAl}_{12}\text{O}_{19}$  ( $\text{CA}_6$ ) were identified in S1, S2 and S3, but there was only a small amount of  $\text{CA}_6$  in S3. Furthermore, almost no  $\text{CA}_6$  was detected in S4. These results indicated that  $\text{Ca}(\text{CH}_3\text{COO})_2\cdot\text{H}_2\text{O}$  infiltrated into the original porous preform had reacted with  $\text{Al}_2\text{O}_3$  at high temperatures, forming  $\text{CA}_6$ . Moreover, along the direction from S1 to S4, the peak intensity of  $\text{CA}_6$  weakened gradually to 0, while the intensities of alumina and MA almost did not change, which further indicated that  $\text{CA}_6$  had been successfully formed in the MA-A matrix, with a graded distribution along the infiltration direction.

**Microstructure of  $\text{CA}_6/(\text{MA-A})$  composites.** Shown in Fig. 4 is a profile of EDS linear scan across the fired composite. The infiltration boundary is clearly seen (Fig. 4a). When the porous preform was

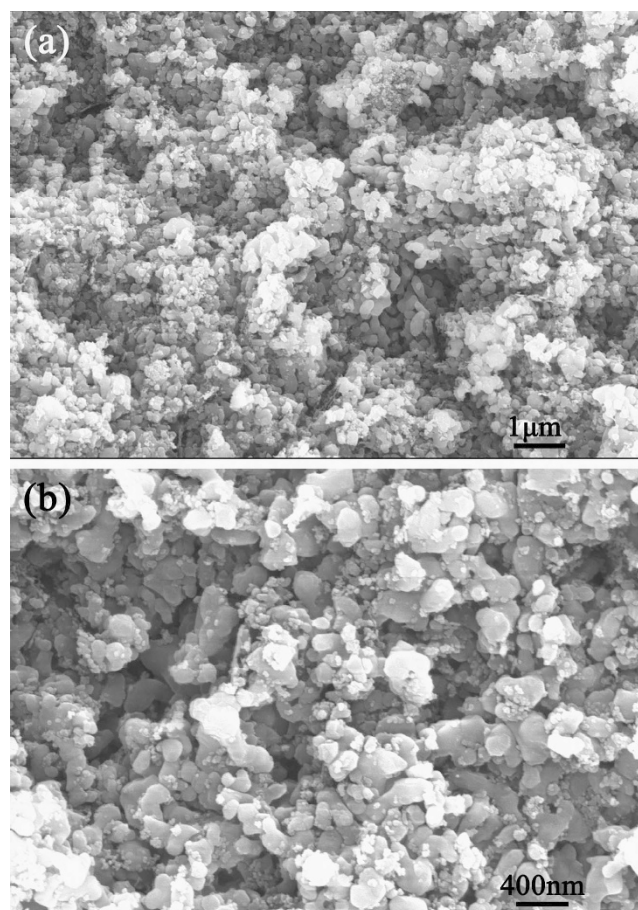


**Figure 2** | SEM images of preform after pre-sintered. (a) low magnification, and (b) high magnification.

partially immersed (1/4 of its length) in a saturated calcium acetate solution, the pressure of cohesion and adhesion which cause the liquid to work against gravity. Due to the capillary action, the infiltration boundary actually had moved beyond the middle line of the sample, as illustrated schematically in Fig. 1. Along the infiltration direction, the intensities of aluminum, magnesium and oxygen almost did not change, whereas the intensity of calcium

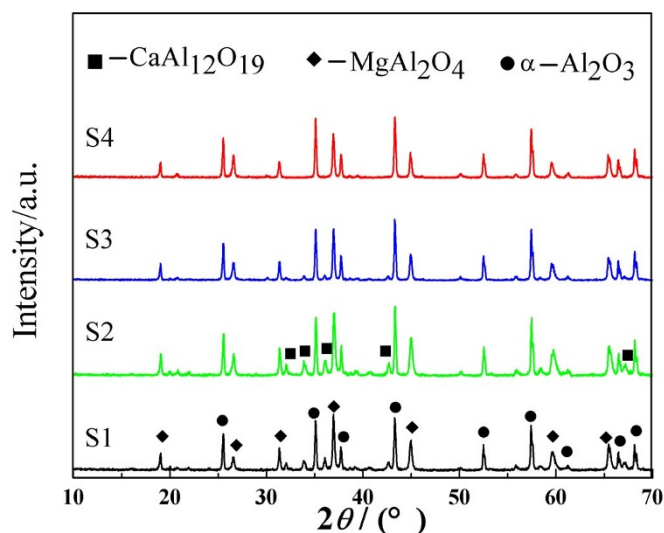


**Figure 3** | XRD patterns of different sections (S1–S4) in the fired graded composite of  $\text{CA}_6/(\text{MA-A})$ .

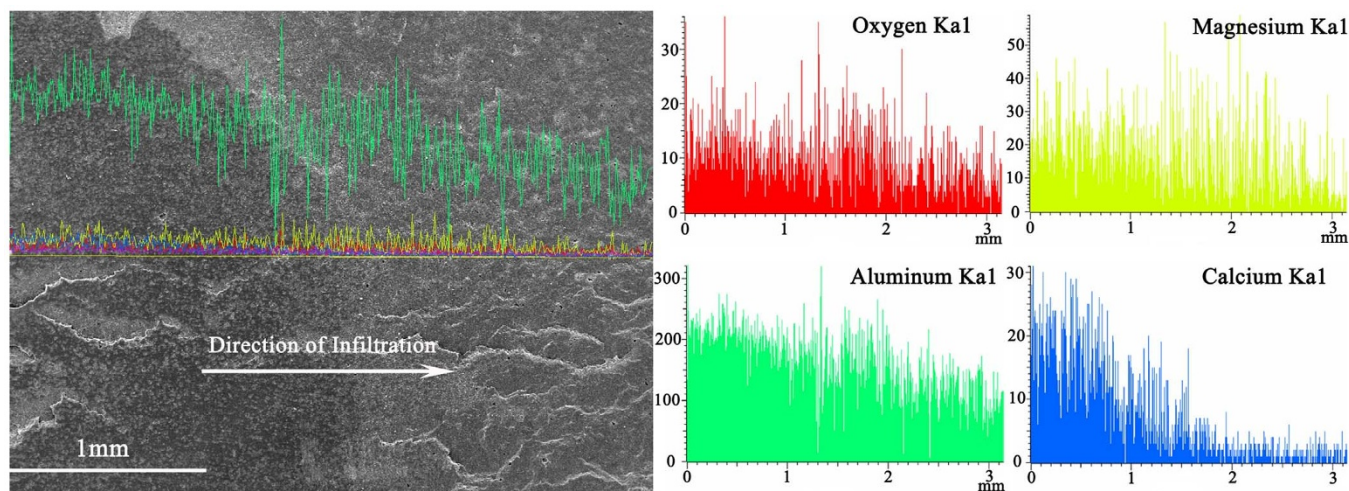


**Figure 4** | EDS linear scan across the fired graded composite of  $CA_6/(MA-A)$ .

initially decreased gradually and then sharply upon crossing the infiltration boundary. These results further verified the graded distribution of calcium in the MA-A matrix.

SEM micrographs shown in Fig. 5 reveal the great effects of  $Ca(CH_3COO)_2 \cdot H_2O$  on the graded microstructure in the fired sample. Lots of 0.5–4  $\mu m$  thick plate-like  $CA_6$  were seen among the alumina and MA grains in S1 and S2 (Fig. 5a & b). The average size of pores between the plate-like  $CA_6$  was  $\sim 0.5 \mu m$ . However, only a few layered structures were observed in S3 (Fig. 5c), and none was seen in S4 (Fig. 5d). On the other hand, in S3 and S4, 3–7  $\mu m$  spherical alumina grains with smooth surfaces were present, and their amount in S3 (Fig. 5c) was less than in S4 (Fig. 5d). Almost no such spherical alumina grains were found in S1 and S2 (Fig. 5a & b), although XRD results (Fig. 5) did indicate the presence of significant amounts of alumina in them. This could be due to two reasons. One was that some spherical alumina had been consumed with the formation of  $CA_6$ , and the other was that alumina grains did not have a spherical morphology in S3 and S4. The formation of  $CA_6$  might have hindered the grain growth of alumina. Tiny MA grains with 0.1–2  $\mu m$  in size and with irregular shapes were present on the

surface and in the original voids among alumina grains. Hence, from the bottom (S1) to the top (S4) in the  $CA_6/(MA-A)$  composites, the formation of layered structure was substantially reduced, concurrent with the gradual increase in the spherical alumina grains.

Figure 6 gives a typical TEM image, along with the corresponding EDS, revealing the coexistence of A, MA and  $CA_6$  in the fired composite sample. Fig. 7 further presents HRTEM images of the three phases. The platelet grains, the translucent particles, and the dark contrast grains were identified to be  $CA_6$ , alumina, and MA (Fig. 6a), respectively, based on Figs. 6(b–d) and Fig. 7. The HRTEM images and SAED patterns reveal the crystal lattice structures of the three phases. EDS (Fig. 6c) verified that MA contained Mg and Al in the molar ratio of 0.41, which is smaller than the stoichiometric ratio (0.50). Moreover, the lattice fringe spacing corresponding to the (200) plane of MA was identified as 0.282 nm (Fig. 7b), which is also slightly different from the value (0.286 nm) in the stoichiometric MA. These are understandable, as the structure and the energetics of the spinels permit them to tolerate a wide range of cation compositions<sup>37–39</sup>. At high temperature MA can form a wide range of solid solutions with excessive magnesia or alumina, i.e.,  $MgO \cdot nAl_2O_3$  [*n*

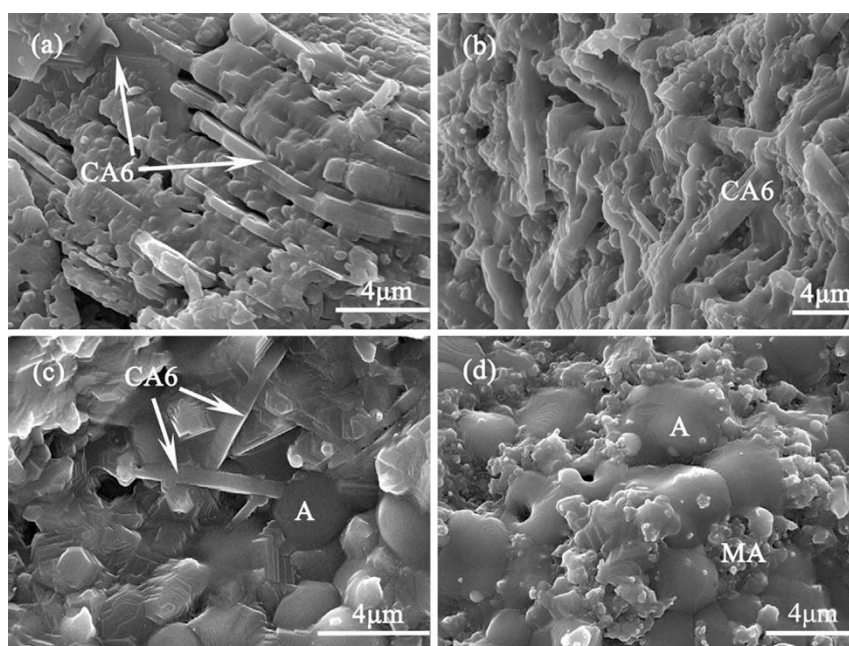


**Figure 5** | Morphologies of different sections in the fired graded composite of  $CA_6/(MA-A)$ . (a) S1, (b) S2, (c) S3, and (d) S4.

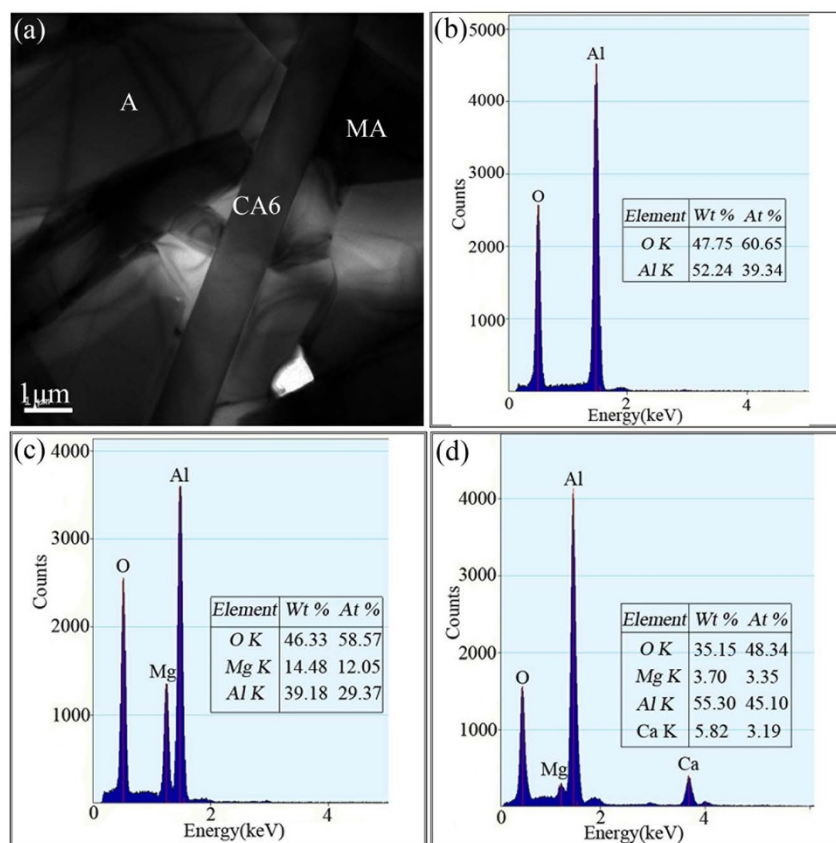


**Figure 6** | TEM micrograph and EDS pattern of the fired composite. (a) A TEM micrograph showing typical morphologies of A, MA, and CA<sub>6</sub> in the fired composite. EDS patterns (b) A, (c) MA, and (d) CA<sub>6</sub>.

= 0.8(MgO rich)-3.5(Al<sub>2</sub>O<sub>3</sub> rich)]<sup>40</sup>. The non-equivalent replacement of Mg<sup>2+</sup> ions (larger ionic radius) with Al<sup>3+</sup> ions (smaller ionic radius) results in the reduction in the unit cell parameter and interplanar spacing<sup>37</sup>. Hence, the results presented above were in the agreement with the theoretical analysis and the dark contrast phases were confirmed as an alumina-rich nonstoichiometric spinel, which could contribute to the improvement in slag resistance<sup>41</sup>.

**Bulk density and mechanical properties of CA<sub>6</sub>/(MA-A) composites.** Bulk density (Fig. 8a) increased gradually in the order from S1 to S4, i.e., along the infiltration direction. It was only 3.60 g·cm<sup>-3</sup> in S1, but increased evidently to 3.78 g·cm<sup>-3</sup> in S4. The theoretical densities of CA<sub>6</sub>, MA and alumina are 3.79 g·cm<sup>-3</sup>, 3.58 g·cm<sup>-3</sup> and 3.97 g·cm<sup>-3</sup>, respectively. As shown in Figs. 3 & 5, and discussed above, the CA<sub>6</sub> content decreased whereas alumina content increased along the infiltration direction (from S1 to S4). The formation of lower density CA<sub>6</sub> at the expense of higher density α-Al<sub>2</sub>O<sub>3</sub> explains the overall density increase along the infiltration direction. In addition, as shown in Fig. 5, high levels of porosity were present between the laminar CA<sub>6</sub> in S1 and S2, which could additionally reduce the bulk density in these two sections.

Vickers hardness and fracture toughness as a function of the distance away from the infiltration end are illustrated in Fig. 8b. Indentations were made at the positions that were respectively 1.9, 6.2, 10.3, 13.9, 15.7, 17.8, 19.8, 22.0, 24.1, 26.3 and 30.1 mm away from the infiltration end. The hardness almost did not change with the distance up to about 14 mm, but started to increase evidently beyond this distance. It eventually leveled-out after increasing the distance >26 mm. At the 1.9 mm distance, the hardness was only 8.78 GPa, but increased markedly to 14.33 GPa at the 24.1 mm

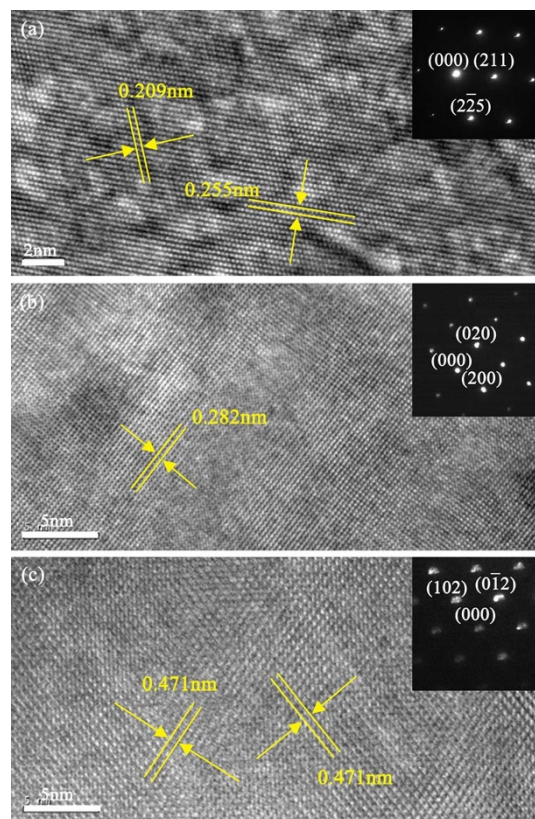


**Figure 7** | HRTEM images and SAED patterns of the fired composite. (a) alumina, (b) spinel, and (c) calcium hexaluminate in the fired composite.

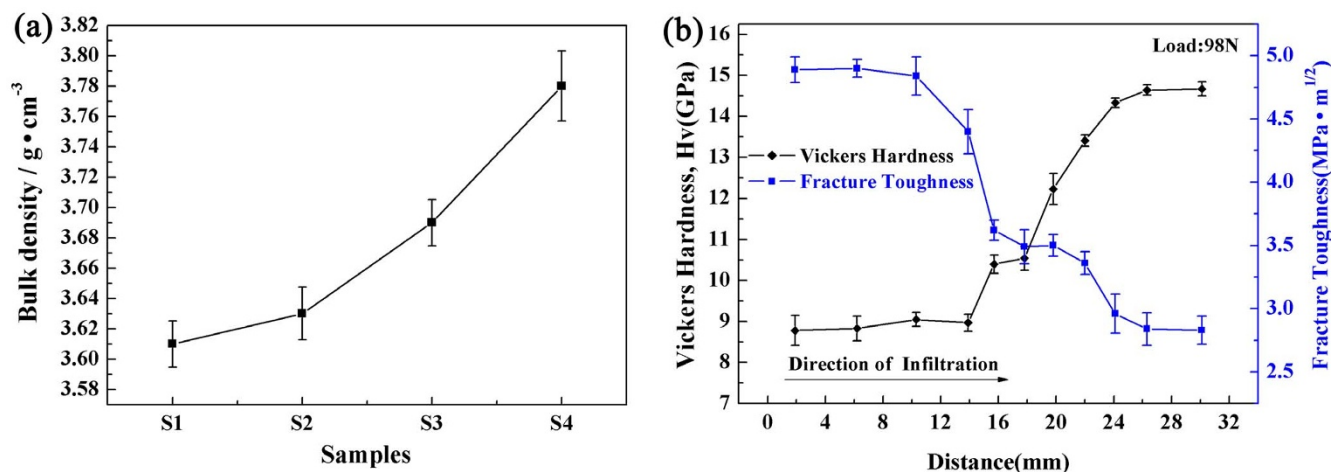


**Figure 8 | The physical and mechanical properties of the fired composite.** (a) Bulk density corresponding to different sections in the fired  $\text{CA}_6/(\text{MA}-\text{A})$  composite. (b) Vickers hardness and fracture toughness of the fired sample as a function of the distance from its infiltration end. The load used was 98 N.

distance and leveled-out thereafter. On the other hand, an opposite trend was seen in the case of fracture toughness. The fracture toughness was  $4.89 \text{ MPa} \cdot \text{m}^{1/2}$  at the 1.9 mm distance, decreased to  $2.96 \text{ MPa} \cdot \text{m}^{1/2}$  at the 24.1 mm distance and leveled-out thereafter. These results corresponded well to the graded distribution of the less hard plate-like  $\text{CA}_6$  along the infiltration direction shown in Fig. 3, Fig. 4 and Fig. 5 and discussed above. Owing to the higher Vickers hardness and density, the MA-A region could play a role in supporting the structure of the composites, whereas the  $\text{CA}_6/(\text{MA}-\text{A})$  region had a better toughness, which could prevent the crack propagation and improve the spalling resistance. In order to assist understanding the toughening mechanism, cracking arising from indentation was further examined by using SEM and TEM.

The path of a crack arising from the indentation on the fired composite is illustrated in Fig. 9a. The crack initiated from the tip area of the indentation and extended forward. A higher magnification SEM micrograph (Fig. 9b) of the area marked in Fig. 9a further reveals crack bridging (labeled as '1'), crack deflection (labeled as '2') and crack cutting through a  $\text{CA}_6$  grain (labeled as '3'). In addition, as revealed by Figure 10, a crack propagated in the composite in both intercrystalline and transcrystalline fracture modes. The crack initiated transgranularly from a place shown at the right side of Fig. 10, then extended along an elongated grain in an intergranular mode, and finally cut through another elongated grain of  $\text{CA}_6$  (identified by EDS (not shown)). In summary, the presence of elongated  $\text{CA}_6$  grains toughened the composite via crack-deflection and crack-bridging mechanisms<sup>14</sup>. This was in accordance with the results described and discussed above (Fig. 8b).

## Discussion

Calcium hexaluminate/magnesio aluminium spinel-alumina [ $\text{CA}_6/(\text{MA}-\text{A})$ ] functionally graded composites with novel microstructures and properties were successfully prepared via infiltration of a porous preform fabricated from  $\alpha\text{-Al}_2\text{O}_3$  and MgO powders with a saturated calcium acetate solution and subsequent sintering at high temperatures. The  $\text{CA}_6$  content in the fired  $\text{CA}_6/(\text{MA}-\text{A})$  composites decreased gradually along the infiltration direction, significantly affecting their microstructure, physical and mechanical properties. Along the direction from the bottom (S1) to the top (S4) of the composite, the formation of layered structure of  $\text{CA}_6$  was substantially reduced, whereas spherical alumina grains increased gradually. Microstructural analysis revealed that MA in the fired composite was an alumina-rich nonstoichiometric spinel with a lower atomic ratio of Mg/Al and a smaller lattice fringe spacing. The presence of  $\text{CA}_6$

had hindered slightly the densification of the MA-A matrix. When the distance from the infiltration end was small (i.e., in the  $\text{CA}_6/(\text{MA}-\text{A})$  section), the hardness changed very little with the distance. However, when the distance was large (i.e., in the MA-A section), it

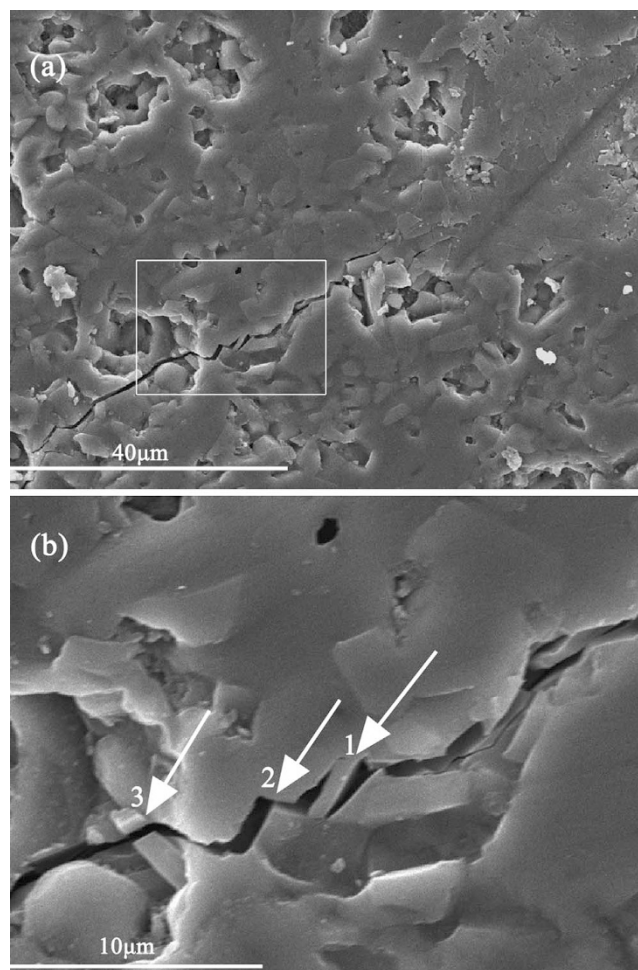


**Figure 9 | SEM images of a typical crack arising from the indentation on the fired composite.** (a) low magnification, and (b) high magnification, showing crack bridging (labeled as '1'), crack deflection (labeled as '2') and crack cutting through a  $\text{CA}_6$  grain (labeled as '3').



**Figure 10** | A TEM image showing crack propagation in the fired composite.

increased evidently with the distance and eventually leveled-out. The MA-A region could play a role in supporting the structure of the composites, because of the higher Vickers hardness and density. The lower Vickers hardness in the  $CA_6$ /(MA-A) region was due to the presence of less hard  $CA_6$ . However, the fracture toughness in this region was higher than in the MA-A region, which could be attributed to the crack-deflection and crack-bridging effects arising from the plate-like  $CA_6$ . This region had a better toughness, which could prevent the crack propagation and improve the spalling resistance. This research not only prepared [ $CA_6$ /(MA-A)] functionally graded composites with novel microstructures and properties that could be used in the areas where the resistances against wear, oxidation, thermal shock, fracture, chemical corrosion and/or heat are required, but also provided a new and simple method that can be applied in fabricating other functional materials with multifunctionalities.

## Methods

The main raw materials used included MgO (purity > 98%, ~0.1 μm, Guangfu Technology Development Co., Ltd., Tianjin, China),  $\alpha$ - $Al_2O_3$  (purity > 99.9%, ~0.4 μm, Xin Meiyu Alumina Co., Ltd., Zibo, Shandong, China) and  $Ca(CH_3COO)_2 \cdot H_2O$  (purity > 98%, Guangfu Fine Chemical Research Institute, Tianjin, China).  $\alpha$ - $Al_2O_3$  and MgO in the molar ratio of 4 : 1 were mixed in a ball mill for 3 h. The powder mixture was placed in a steel die and uniaxially pressed at 50 MPa, forming a bar sample of  $5 \times 6 \times 45$  mm. The bar sample was pre-fired at 1100 °C for 2 h to increase its strength while still maintaining a sufficient level of porosity in it for the later infiltration. Such a porous preform was partially immersed (1/4 of its length) in a saturated calcium acetate solution at room temperature for 0.5 h. The infiltrated preform, after being dried at room temperature for 24 h, was heated in an electric furnace at 1400 °C for 10 h (to allow  $CA_6$  platelets to grow) and further fired at 1600 °C for 4 h before furnace-cooling to room temperature. Open porosity of preform and bulk density of the resultant sample were determined based on the Archimedes' principle, and its Vickers hardness measured under a load of 98 N for 10 s. The half-diagonal lengths and the radial surface crack lengths were measured using a micrometer attached to the sample stage, and their averages were taken for the hardness and fracture toughness calculations.

Phases in the fired samples were identified by an X-ray diffractometer (XRD; XD-3, Purkinje General Instrument Co., Ltd) using  $Cu K\alpha_1$  radiation ( $\lambda = 1.5406 \text{ \AA}$ ) with a scanning rate of  $8^\circ \text{ min}^{-1}$ , and their microstructures observed by a scanning electron microscope (SEM; JEM-6460 LV microscope, Japan), and a transmission electron microscope (TEM, FEI-Tecnai-G2-F20, Philips, Netherlands) equipment with an energy dispersive spectroscopy (EDS, INCA, Oxford Instrument, UK) and selected area electron diffraction (SAED). Thin slices of samples for TEM observations were cut from the fired sample with a diamond wire, mechanically pre-thinned, and ion-milled.

- Păcurariu, C. *et al.* New synthesis methods of  $MgAl_2O_4$  spinel. *J. Eur. Ceram. Soc.* **27**, 707–710 (2007).
- Braulio, M. A. L., Rigaud, M., Buhr, A., Parr, C. & Pandolfelli, V. C. Spinel-containing alumina-based refractory castables. *Ceram. Int.* **37**, 1705–1724 (2011).
- De Aza, A. H., Pena, P. & De Aza, S. Ternary system  $Al_2O_3$ -MgO-CaO: part I, primary phase field of crystallization of spinel in the subsystem  $MgAl_2O_4$ - $CaAl_4O_7$ -CaO-MgO. *J. Am. Ceram. Soc.* **82**, 2193–2203 (1999).
- Rufner, J., Anderson, D., van Benthem, K. & Castro, R. H. R. Synthesis and sintering behavior of ultrafine (10 nm) magnesium aluminate spinel nanoparticles. *J. Am. Ceram. Soc.* **96**, 2077–2085 (2013).
- Mazzoni, A. D., Sainz, M. A., Caballero, A. & Aglietti, E. F. Formation and sintering of spinels ( $MgAl_2O_4$ ) in reducing atmospheres. *Mater. Chem. Phys.* **78**, 30–37 (2002).
- Wahsh, M. M. S., Khattab, R. M. & Awaad, M. Thermo-mechanical properties of mullite/zirconia reinforced alumina ceramic composites. *Mater. Des.* **41**, 31–36 (2012).
- Mohapatra, D. & Sarkar, D. Preparation of MgO-MgAl<sub>2</sub>O<sub>4</sub> composite for refractory application. *J. Mater. Process. Technol.* **189**, 279–283 (2007).
- Ping, L. R., Azad, A. M. & Dung, T. W. Magnesium aluminate ( $MgAl_2O_4$ ) spinel produced via self-heat-sustained (SHS) technique. *Mater. Res. Bull.* **36**, 1417–1430 (2001).
- Naghizadeh, R., Rezaie, H. R. & Golestani-Fard, F. Effect of  $TiO_2$  on phase evolution and microstructure of  $MgAl_2O_4$  spinel in different atmospheres. *Ceram. Int.* **37**, 349–354 (2011).
- Sarkar, R. & Banerjee, G. Effect of addition of  $TiO_2$  on reaction sintered MgO- $Al_2O_3$  spinels. *J. Eur. Ceram. Soc.* **20**, 2133–2141 (2000).
- Ghosh, A., Das, S. K., Biswas, J. R., Tripathi, H. S. & Banerjee, G. The effect of ZnO addition on the densification and properties of magnesium aluminate spinel. *Ceram. Int.* **26**, 605–608 (2000).
- Sarkar, R., Das, S. K. & Banerjee, G. Effect of additives on the densification of reaction sintered and presynthesised spinel. *Ceram. Int.* **29**, 55–59 (2003).
- Sarkar, R., Das, S. K. & Banerjee, G. Effect of addition of  $Cr_2O_3$  on the properties of reaction sintered MgO- $Al_2O_3$  spinels. *J. Eur. Ceram. Soc.* **22**, 1243–1250 (2002).
- Rani, D. A., Yoshizawa, Y., Hirao, K. & Yamauchi, Y. Effect of rare-earth dopants on mechanical properties of alumina. *J. Am. Ceram. Soc.* **87**, 289–292 (2004).
- Buban, J. P. *et al.* Grain boundary strengthening in alumina by rare earth impurities. *Science* **311**, 212–215 (2006).
- Ji, Y. & Yeomans, J. A. Processing and mechanical properties of  $Al_2O_3$ -5 vol.% Cr nanocomposites. *J. Eur. Ceram. Soc.* **22**, 1927–1936 (2002).
- An, L., Ha, H. C. & Chan, H. M. High-strength alumina/alumina-calcium hexaluminate layer composites. *J. Am. Ceram. Soc.* **81**, 3321–3324 (1998).
- Low, I. M., Skala, R., Richards, R. & Perera, D. S. Synthesis and properties of novel mullite/zirconia-toughened alumina composites. *J. Mater. Sci. Lett.* **12**, 1585–1587 (1993).
- Sommer, F., Landfried, R., Kern, F. & Gadow, R. Mechanical properties of zirconia toughened alumina with 10–24 vol.% 1.5 mol% Y-TZP reinforcement. *J. Eur. Ceram. Soc.* **32**, 3905–3910 (2012).
- Yamamoto, G., Omori, M., Hashida, T. & Kimura, H. A novel structure for carbon nanotube reinforced alumina composites with improved mechanical properties. *Nanotechnology* **19**, 315708 (2008).



21. Yamamoto, G. Nanotube fracture during the failure of carbon nanotube/alumina composites. *Carbon* **49**, 3709–3716 (2011).
22. Liu, J., Yan, H. X. & Jiang, K. Mechanical properties of graphene platelet-reinforced alumina ceramic composites. *Ceram. Int.* **39**, 6215–6221(2013)
23. Centeno, A. *et al.* Graphene for tough and electroconductive alumina ceramics. *J. Eur. Ceram. Soc.* **33**, 3201–3210 (2013).
24. Liu, J., Yan, H. X., Reece, M. J. & Jiang, K. Toughening of zirconia/alumina composites by the addition of graphene platelets. *J. Eur. Ceram. Soc.* **32**, 4185–4193 (2012).
25. Kwon, H., Cho, S., Leparoux, M. & Kawasaki, A. Dual-nanoparticulate-reinforced aluminum matrix composite materials. *Nanotechnology* **23**, 225704 (2012).
26. Vishista, K. & Gnanam, F. D. Sol-gel synthesis and characterization of alumina-calcium hexaaluminate composites. *J. Am. Ceram. Soc.* **88**, 1175–1179 (2005).
27. Wang, W. L. *et al.* Microstructure and mechanical properties of alumina ceramics reinforced by boron nitride nanotubes. *J. Eur. Ceram. Soc.* **31**, 2277–2284 (2011).
28. Chen, P. L. & Chen, I. W. In situ alumina/aluminate platelet composites. *J. Am. Ceram. Soc.* **75**, 2610–2612 (1992).
29. De La Iglesia, P. G., Moreno, O. G., Torrecillas, R. & Menéndez, J. L. Influence of different parameters on calcium hexaaluminate reaction sintering by spark plasma. *Ceram. Int.* **38**, 5325–5332 (2012).
30. Sako, E. Y., Braulio, M. A. L., Zinngrebe, E., van der Laan, S. R. & Pandolfelli, V. C. In-depth microstructural evolution analyses of cement-bonded refractory castables: novel insights regarding spinel and CA<sub>6</sub> formation. *J. Am. Ceram. Soc.* **95**, 1732–1740 (2012).
31. Asmi, D. & Low, I. M. Self-reinforced Ca-hexaluminate alumina composites with graded microstructures. *Ceram. Int.* **34**, 311–316 (2008).
32. Marple, B. R. & Green, D. J. Mullite alumina particulate composites by infiltration processing: II, infiltration and characterization. *J. Am. Ceram. Soc.* **73**, 3611–3616 (1990).
33. Suresh, S. Graded materials for resistance to contact deformation and damage. *Science* **292**, 2447–2451 (2001).
34. Pratapa, S., Low, I. M. & O'connor, B. H. Infiltration-processed, functionally graded aluminium titanate/zirconia-alumina composite: part I microstructural characterization and physical properties. *J. Mater. Sci.* **33**, 3037–3045(1998).
35. Asmi, D. & Low, I. M. Infiltration and physical characteristics of functionally graded alumina/calcium hexaluminate composites. *J. Mater. Process. Technol.* **118**, 225–230 (2001).
36. Pratapa, S. & Low, I. M. Infiltration-processed, functionally graded aluminium titanate zirconia-alumina composite: part II mechanical properties. *J. Mater. Process. Technol.* **33**, 3047–3053 (1998).
37. Raj, R., Saha, A., An, L., Hasselman, D. P. H. & Ernst, P. Ion exchange at a metal-ceramic interface. *Acta Mater.* **50**, 1165–1176 (2002).
38. Yu, Y., Mark, J., Ernst, F., Wagner, T. & Raj, R. Diffusion reactions at Al-MgAl<sub>2</sub>O<sub>4</sub> interfaces—and the effect of applied electric fields. *J. Mater. Sci.* **41**, 7785–7797(2006).
39. Singh, G., Yu, Y., Ernst, F. & Raj, R. Shear strength and sliding at a metal-ceramic (aluminum-spinel) interface at ambient and elevated temperatures. *Acta Mater.* **55**, 3049–3057(2007).
40. Sutorik, A. C. *et al.* Transparent solid solution magnesium aluminate spinel polycrystalline ceramic with the alumina-rich composition MgO·1.2Al<sub>2</sub>O<sub>3</sub>. *J. Am. Ceram. Soc.* **95**, 636–643 (2012).
41. Sarpoolaky, H., Zhang, S. & Lee, W. E. Corrosion of high alumina and near stoichiometric spinels in iron-containing silicate slags. *J. Eur. Ceram. Soc.* **23**, 293–300 (2003).

## Acknowledgments

This work was financially supported by the National Natural Science Foundation of China (NSFC Grant Nos. 51072186 and 51032007) and the Fundamental Research Funds for the Central Universities (Grant No. 2652014039).

## Author contributions

S.Y., J.T.H. and Z.H.H. conceived and designed the experiments. S.Y. and J.T.H. carried out the experiments. S.Y., Y.G.L. and M.H.F. analyzed the data. All authors discussed the results. S.Y., J.T.H., Z.H.H. and S.W.Z. wrote the paper.

## Additional information

**Competing financial interests:** The authors declare no competing financial interests.

**How to cite this article:** Yi, S. *et al.* Novel calcium hexaluminate/spinel-alumina composites with graded microstructures and mechanical properties. *Sci. Rep.* **4**, 4333; DOI:10.1038/srep04333 (2014).



This work is licensed under a Creative Commons Attribution-NonCommercial-NoDerivs 3.0 Unported license. To view a copy of this license, visit <http://creativecommons.org/licenses/by-nc-nd/3.0>